Meteorologische Zeitschrift, Vol. **14**, No. 5, 609-626 (October 2005)

Article

Advanced Radar Wind Profiling

ANDREAS MUSCHINSKI[1], VOLKER LEHMANN[2], LUTZ JUSTEN[3] and GERD TESCHKE[3]

[1]Department of Electrical and Computer Engineering, University of Massachusetts, Amherst, Massachusetts, USA
[2]Meteorologisches Observatorium Lindenberg, Deutscher Wetterdienst, Lindenberg, Germany
[3]Zentrum für Technomathematik, Universität Bremen, Germany

(Manuscript received May 10, 2005; in revised form July 11, 2005; accepted July 11, 2005)

Abstract

During the last three decades, radar wind profiling (RWP) has evolved into a key technology for atmospheric science and operational meteorology. In this tutorial status report, RWP is divided into three distinct areas: single-signal RWP, two-signal RWP, and multi-signal RWP. While single-signal RWP, or standard RWP, is a mature technology in many respects, there is still much room for improvement, particularly in the interpretation of signals that are severely contaminated by radio interference or by clutter from aircraft, birds, hydrometeors, etc. Two-signal RWP, the best known examples of which are the spaced-antenna (SA) and frequency-domain interferometry (FDI) techniques, have been used to overcome some of the limitations inherent in standard RWP. Multi-signal RWP is, to a large extent, still unexplored territory. This paper attempts to provide a coherent conceptual framework of advanced RWP and to identify areas of future research and development.

Zusammenfassung

Im Laufe der letzten drei Jahrzehnte hat sich Radar-Windprofiling (RWP) zu einer Schlüsseltechnologie in der Atmosphärenforschung und der operationellen Meteorologie entwickelt. Im Rahmen einer einführenden Bestandsaufnahme wird RWP in drei Kategorien eingeteilt: Einzel-Signal-RWP, Zwei-Signal-RWP und Multi-Signal-RWP. Obwohl Einzel-Signal-RWP, d.h. Standard-RWP, in vielerlei Hinsicht eine ausgereifte Technologie ist, gibt es dennoch Verbesserungsmöglichkeiten, insbesondere hinsichtlich der Auswertung von Messungen, die durch Radio-Einstreuung oder Störechos von Flugzeugen, Vögeln, Hydrometeoren usw. stark beeinträchtigt sind. Zwei-Signal-RWP, als deren Hauptvertreter die Technik der versetzten Antennen und die Frequenzbereich-Interferometrie gelten können, haben sich als hilfreich zur Überwindung einiger Limitierungen der Standard-RWP erwiesen. Multi-Signal-RWP hingegen ist im wesentlichen noch unbekanntes Territorium. Dieser Beitrag versucht, einen einheitlichen begrifflichen Rahmen der fortgeschrittenen RWP-Technologie zu liefern. Zudem werden mögliche Bereiche zukünftiger Forschung und Entwicklung aufgezeigt.

1 Introduction

The era of radar wind profiling (RWP) began with the pioneering paper by WOODMAN and GUILLÉN (1974), who were the first to demonstrate that the extremely weak VHF radio-wave echoes from clear-air refractive-index perturbations in the troposphere and stratosphere are indeed measurable and that the temporal changes of these echoes can be used to retrieve wind velocities.

Within one decade, the first RWP network, called the Colorado wind-profiling network (STRAUCH et al., 1984), was implemented and provided quasi-operational wind data. The network consisted of four VHF profilers operating at 50 MHz (wavelength 6 m) and one UHF profiler operating at 915 MHz (wavelength 33 cm). According to STRAUCH et al. (1984, p. 37), one objective of that program was "to develop tropospheric wind-profiling radars that will provide vertical profiles of the horizontal wind throughout the troposphere, operate in nearly all weather conditions, provide wind data automatically and continuously with unattended operation, be suitable for widespread use in networks, provide data for mesoscale and synoptic scale applications." The design goal was "to provide vertical profiles of the horizontal wind with accuracy of orthogonal components to better than 1 $\mathrm{m\,s^{-1}}$; height resolution of 100 m below 600 mb, 300 m to 300 mb, and 1 km to 100 mb; temporal resolution of 15 min for profiles to 600 mb, 30 min for profiles to 300 mb, and 60 min for profiles to 100 mb." The design goals for operational RWPs have barely changed during the last twenty years, which in hindsight may be seen as an indication that the problems encountered in RWP are more serious and complicated than originally anticipated.

The Colorado network was the precursor of the National Oceanic and Atmospheric Administration's (NOAA) National Profiler Network (BARTH et al., 1994), which has been operating continuously since

*Corresponding author: Andreas Muschinski, Dept. of Electrical and Computer Engineering, University of Massachusetts at Amherst, 151 Holdsworth Way, Amherst, MA 01003-9284, U.S.A., e-mail: muschinski@ecs.umass.edu

0941-2948/2005/0067 $ 8.10
DOI: 10.1127/0941-2948/2005/0067

1992, and by the end of 2004 consisted of 35 RWP sites across the United States. Similar RWP networks are now operating in Europe and Japan.

Today, there are hundreds of research and operational RWPs worldwide, measuring wind velocities in the atmospheric boundary layer, the free troposphere, and in the lower stratosphere. Overviews of the technical and scientific aspects of RWP have been provided, among others, by Gage (1990), RÖTTGER and LARSEN (1990), DOVIAK and ZRNIĆ (1993), and MUSCHINSKI (2004). Based on the overall success of RWPs, many consider RWP a mature technology. A closer look at the underlying physical and mathematical principles, however, reveals that there is still room for substantial improvement and further development. Major progress can be anticipated in two directions. First, traditional RWP, or single-signal RWP, can be made more efficient by taking advantage of new methods in mathematical signal analysis. Second, two-signal and multi-signal RWP techniques, which have been studied by researchers for many years but have not yet entered the operational arena, offer a wide range of options to overcome limitations that are inherent to single-signal RWP.

The purpose of this paper is to give a tutorial overview of single-signal, two-signal, and multi-signal radar wind profiling. Emphasis is placed on the physical and mathematical concepts. Examples of RWP measurements are presented in order to give an impression of the wide variety of problems that arise from non-atmospheric signal contributions, i.e., clutter and noise.

The paper is organized as follows. Section 2 gives an overview of the physical nature of a single RWP signal. The RWP signal is divided into a clear-air component, a clutter component, and a noise component. Basic single-signal statistics are introduced and explained, among them the so-called Doppler spectrum and its first three moments. A number of the difficulties to retrieve clear-air statistics from contaminated RWP signals are explained. Limitations inherent to single-signal RWP are discussed. Section 3 reviews two-signal RWP techniques, mainly the spaced-antenna technique and the frequency-domain interferometry technique. Section 4 gives an introduction to multi-signal RWP, which is mathematically much more demanding than single-signal and two-signal RWP. A wide variety of forward problems can be formulated, and the associated inverse problems will remain a fertile research area in the foreseeable future. A summary and a brief outlook are given in Section 5.

2 Single-signal radar wind profiling

This section describes physical, technological, and mathematical aspects of single-signal RWP. Section 2.1 illustrates the nature of RWP signals on the basis of a measurement example. Section 2.2 describes and discusses the various sources of clutter and noise, which often dominate the clear-air echo and make it difficult, sometimes impossible, to retrieve wind information from a measured RWP signal. Based on the measurement example of Section 2.1, Section 2.3 introduces the Doppler spectrum and explains why RWPs can measure wind velocities at signal-to-noise ratios as low as -35 dB or even lower. Section 2.4 summarizes the theory that relates the intensity of the clear-air echo to the spatial spectrum of the refractive-index perturbations in the RWP's sampling volume. The relationship between Doppler shift and wind velocity has been analyzed only recently on the basis of first-principle theory, as summarized in Section 2.5. Of considerable practical importance for single-signal RWP are new mathematical time-frequency decomposition techniques. Section 2.6 illustrates the efficacy of these techniques by means of an RWP signal that is severely contaminated by an aircraft echo.

2.1 A measurement example

Figure 1 shows the time series of the real and imaginary parts of a single signal measured with the east beam of the 482-MHz profiler operated by the Deutscher Wetterdienst (DWD, German Weather Service) at its Meteorologisches Observatorium Lindenberg (MOL). The data were taken on Dec. 1, 1999, with the east beam (15^{o} off zenith) at a height of 3035 m MSL. The elevation of the MOL site is 103 m MSL.

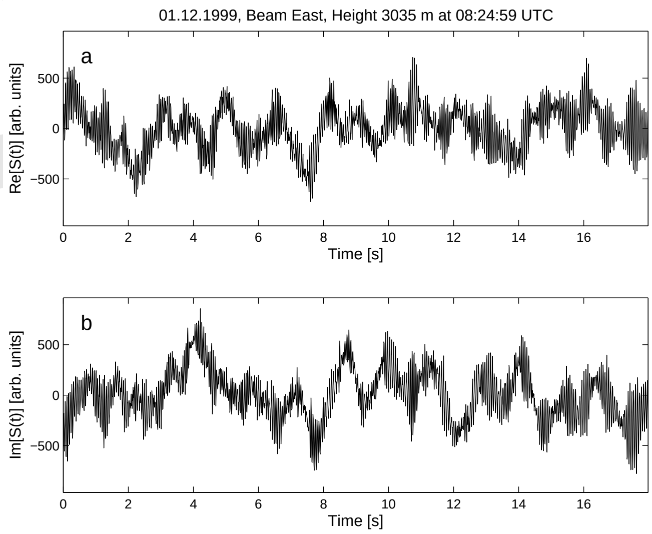

Figure 1: Time series of the in-phase (a) and quadrature (b) component of a signal measured on 1 December 1999 with the 482-MHz RWP at the Meteorologisches Observatorium Lindenberg, Germany. Each of the two time series contains 2048 samples. Each sample is the coherent sum of 144 echoes from subsequent pulses.

The real (in-phase) part and the imaginary (quadrature) part of the complex time series each contain 2048 samples. Each sample is the coherent average of the echoes from 144 subsequent pulses. That is, the data are the result of 294,912 subsequent pulses and their respective echoes. The interpulse (or interecho) period was 61 μs, such that the coherent-integration time was 8.8 ms, and the length of the entire time series (the "dwell time") was 18.0 s. (Note that some authors use the term "dwell time" as the time during which the radar "dwells" in the same beam-pointing direction; that definition may or may not coincide with our definition.)

The coherent-integration time must be short compared to the time scales at which the signal's phase and amplitude change significantly due to the mean and turbulent motion of the atmospheric refractive-index perturbations in the RWP's resolution volume. For RWP operating in the lower UHF regime, where the radar wavelength is of order 1 m, a coherent-integration time of order 10 ms are usually a good choice.

Figure 2 shows the first second of the 18-s-long signal time series presented in Figure 1. The signal fluctuations at time scales of order 50 ms are due to echoes from atmospheric refractive-index perturbations while the fluctuations at one-second time scales, which dominate Figure 1, are caused by clutter from slowly moving objects on the ground.

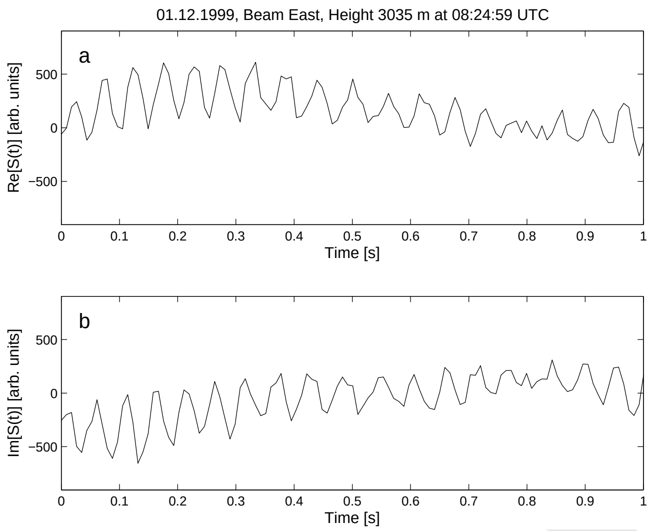

Figure 2: The first second of the signal time series shown in Figure 1

2.2 Definitions: Clutter, noise, and clear-air signal

In Figure 2, the clear-air component can be clearly recognized as the nearly sinusoidal oscillations superposed on the slowly changing clutter component. Uncorrelated noise has been substantially suppressed because of the coherent averaging. If the single echoes were shown instead of the coherently added echoes, then Figure 2 would have been noise-dominated, as we will show in the next subsection. (For the data shown in Figure 2 the coherent adding, or averaging, had been done with hardware, and because of hardware limitations the single-echo samples could not be saved; therefore, the single-echo samples cannot be shown here.) The clutter, however, which dominates Figure 1 and in this case is much stronger than the atmospheric echo, cannot be reduced by coherent averaging.

At this point, it is helpful to define the terms clutter, noise, and signal more clearly. Unfortunately, the term "signal" is used in the literature with two different meanings. In the context of "signal processing," "signal" stands for "measured receiver output," which is the sum of clutter, noise, and atmospheric echo. Often, however, "signal" is used synonymously with "atmospheric echo." In the following, we avoid this ambiguity by using the terms "total signal" $S(t)$, "clear-air signal" $I(t)$, clutter $C(t)$, and noise $N(t)$:

$$S(t) = I(t) + C(t) + N(t), \tag{2.1}$$

where all terms are complex-valued "base-band" currents measured at the receiver output. Our definition of $I(t)$ is identical to the one in DOVIAK and ZRNIĆ (1984), DOVIAK and ZRNIĆ (1993, eq. 11.115 on p. 456), and MUSCHINSKI (2004).

Clutter is the totality of undesired echoes. In the case of RWP, clutter includes echoes from airborne objects such as aircraft, birds, bats, insects, atmospheric plankton, airborne debris, hydrometeors, and moving or nonmoving objects on the ground like buildings, power lines, trees, cars, or wind turbines. Whether or not clutter is easily distinguishable from clear-air signals depends on the distribution of the echoing objects in space and time, and on their radial velocities. Insect echoes, for example, are difficult to distinguish from clear-air echoes because insects constitute a "distributed target" (there are often many insects in the same sampling volume), and often they are passively advected with the local wind velocity. The same is true for small rain droplets or small snowflakes. From a purely practical point of view, particularly if one is interested only in wind measurements, there is no need to distinguish between the clear-air component and the clutter component if one can safely assume that the sources of airborne clutter are passively advected with the wind.

We define noise as the sum of all contributions to $S(t)$ that are not the result of an echoing mechanism. From this definition it follows that noise is independent of the strength, the shape, or the transmit time of the transmitted pulses. Noise includes thermal noise in the RWP system, electromagnetic radiation from the sun or other astronomical objects (cosmic noise), and radio signals transmitted from satellites, mobile phones, electrical machinery, etc. (radio interference). It is usually assumed that system noise and cosmic noise are well approximated by a flat “noise floor” (white noise) in the spectrum.

Because clear-air signal, clutter, and noise are uncorrelated from each other, such that $\langle I^*C \rangle = 0$, $\langle I^*N \rangle = 0$, and $\langle C^*N \rangle = 0$ (the angle brackets mean “expectation value of”), the “total Doppler spectrum,” i.e., the frequency spectrum of $S(t)$, is simply the sum of the frequency spectra of $I(t)$, $C(t)$, and $N(t)$, respectively:

$$\phi_S(\omega) = \phi(\omega) + \phi_C(\omega) + \phi_N(\omega), \qquad (2.2)$$

where $\phi(\omega)$ is the spectrum of the clear-air signal, $\phi_C(\omega)$ is the clutter spectrum, and $\phi_N(\omega)$ is the noise spectrum. We have suppressed the subscript “I” in $\phi(\omega)$ in order to keep the notation in the analytical Sections 2.5 and 3.1 simple.

2.3 Measurement example: Periodogram, Doppler spectrum, and signal-to-noise ratio

Figure 3 shows the periodogram of the signal time series presented in Figure 1. The periodogram was computed by means of a Fast Fourier Transform (FFT) algorithm. As is customary in the RWP community, we present the periodogram as a function of frequency $f = \omega/2\pi$ and not of cycle frequency ω. Three features can be clearly distinguished from each other: a peak centered at $f = -18$ Hz, a second peak at $f = 0$, and noise spread over the entire resolvable frequency interval. The resolvable frequencies range from $-f_{\mathrm{Ny}}$ to $+f_{\mathrm{Ny}}$, where

$$f_{\mathrm{Ny}} = \frac{1}{2T_c} \qquad (2.3)$$

is the Nyquist frequency and T_c the coherent-integration time. In our case, T_c = 8.8 ms, which leads to f_{Ny} = 56.9 Hz, in agreement with the frequency range depicted in Figure 3. The frequency increment in a periodogram is

$$\Delta f = \frac{1}{T_d}, \qquad (2.4)$$

where T_d is the dwell time, in our example T_d = 18 s, such that Δf = 0.056 Hz. That is, in Figure 3 a frequency interval of width 10 Hz (like the width of the peak centered at -18 Hz) is represented by 180 points in the periodogram.

A clear distinction has to be made between the periodogram, which can be *calculated* from a finite time series, and the power spectrum, which can only be *estimated* from a finite time series. Definitions of the power spectrum and the cross-spectrum of complex-valued, random variables can be found, e.g., in MUSCHINSKI (2004). Sometimes, the power spectrum is referred to as the auto-spectrum (as opposed to the cross-spectrum), the variance spectrum (because integration over all frequencies gives the variance), or simply as the spectrum.

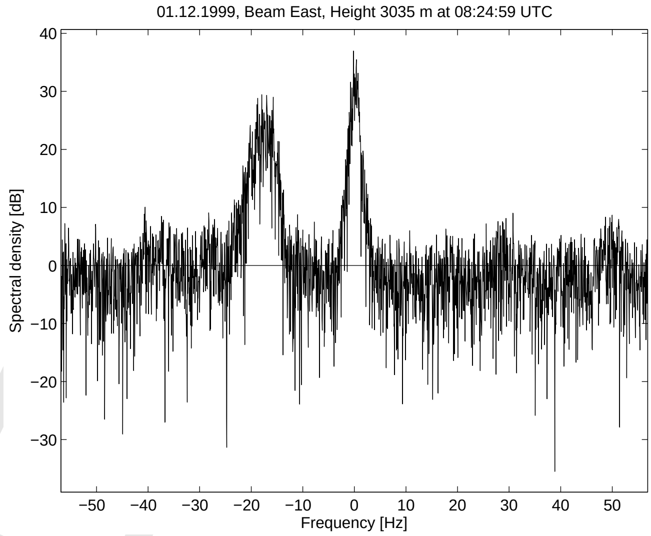

Figure 3: Periodogram of the RWP signal shown in Fig. 2.1.

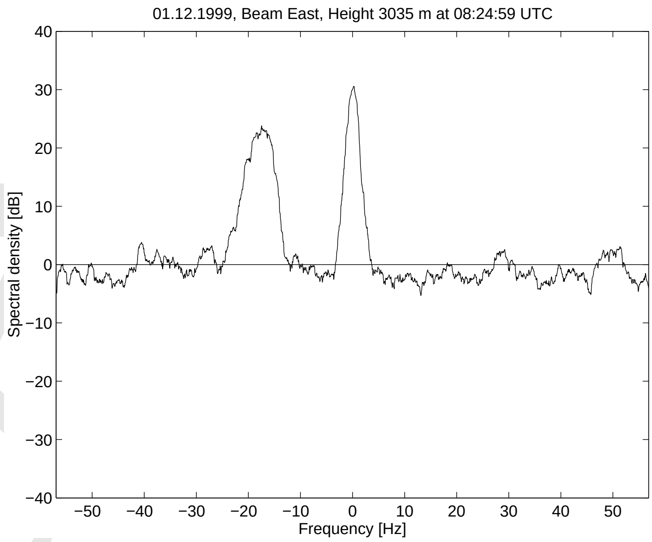

Figure 4: Doppler spectrum, estimated from the periodogram in Figure 3 after averaging in the frequency domain over 20 adjacent spectral points.

The most obvious difference between a periodogram and a spectrum is that in a periodogram the individual spectral points show a random behaviour, sometimes referred to as “speckle,” while a spectrum is usually smooth. Figure 4 shows the periodogram in Figure 3 after averaging over 20 adjacent spectral points, that is, over frequency intervals of 1.1 Hz. Obviously, smoothing reduces the speckle, such that a smoothed periodogram is a better approximation of the spectrum than the “raw” periodogram. It is important to note that the periodogram calculated from a finite data set is a *biased* estimator of the power spectrum (e.g., DOVIAK and ZRNIĆ, 1993, p. 99).

The noise spectral density, ϕ_N, has been estimated with the HILDEBRAND and SEKHON (1974) algorithm and is depicted by the horizontal lines in Figures 3 and 4.

The algorithm does not require any *a priori* knowledge about which parts of the periodogram are pure white noise and which are not, as long as there are a sufficient number of periodogram points that represent pure white noise.

The peak at -18 Hz (correponding to an oscillation period of 56 ms, as visible in the time series in Figure 1) is the atmospheric signal while the peak at zero Doppler shift is ground clutter. The spectral densities in Figures 3 and 4 are given relative to the mean noise spectral density ϕ_N, such that the actual noise spectral density (as a function of frequency) fluctuates around 0 dB. The peak spectral densities of the clear-air signal and the clutter are 23 dB and 30 dB, respectively, above the noise floor in this measurement example.

Let us estimate the signal-to-noise ratio (SNR) of the clear-air signal:

$$SNR = \frac{\langle |I|^2 \rangle}{\langle |N|^2 \rangle}, \tag{2.5}$$

where I is the non-averaged clear-air component and N is the non-averaged noise. The width of the clear-air peak is about 10 Hz, while the Nyquist interval of the non-averaged echoes is $1/(61\mu\mathrm{s})$ = 16.4 kHz, or 2×144 times the Nyquist frequency of the coherently averaged samples, which we showed is 56.9 Hz. That is, the noise is spread over a frequency interval that is about 1600 times as wide as the bandwidth of the atmospheric signal. We found that the variance contained in the "wind peak" (the peak centered at -18 Hz) is higher by 8.7 dB than the variance contained in the noise of the 144-pulse averages. Because the noise energy of single pulses is 144 times larger than the noise energy in the 144-pulse averages, the SNR is by a factor of 144, or by 21.6 dB, lower than 8.7 dB. That is, the SNR in our measurement example is -12.9 dB.

As stated above, in our measurement example the peak spectral density of the clear-air signal is 23 dB above the noise floor, such that the clear-air peak were still 3 dB above the noise floor if the SNR were by 20 dB lower. In other words, the RWP could provide meaningful wind estimates for SNRs as low as -32.9 dB. Moreover, if the bandwidth of the clear-air signal were only 1 Hz (instead of order 10 Hz, as in our example), which is not uncommon under low-turbulence conditions and for shorter dwell times, then the Lindenberg 482-MHz RWP could provide meaningful wind data even if the SNR were as small as -42.9 dB.

The main reason why RWPs can provide meaningful data at extremely low SNRs is that the bandwidth of the clear-air signal is typically by three or more orders of magnitude smaller than the very wide Nyquist interval associated with the very short interpulse period.

Ground clutter has a peak spectral density that often exceeds the clear-air peak spectral density. In that case, ground clutter can be separated from the atmospheric signal only if, as in Figures 3 and 4, their spectra do not overlap.

2.4 Radio-wave propagation theory: Backscattered power from turbulent refractive-index perturbations in the optically clear air

RWP signals can be fully understood only on the basis of the theory of radio-wave propagation through the turbulent atmosphere. This theory, pioneered by TATARSKII (1961), is a synthesis of Maxwell's electromagnetic theory and classical turbulence theory (KOLMOGOROV, 1941; BATCHELOR, 1953).

For single scatter, that is, under the assumption that the first-order Born approximation is valid, the instantaneous clear-air signal $I(t)$ is unambiguously determined by the field of the instantaneous refractive-index perturbations, $n(\mathbf{x}',t)$, in the RWP's resolution volume through an equation of the form

$$I(t) = \iiint G(\mathbf{x}')\, n(\mathbf{x}',t)\, d^3x' \tag{2.6}$$

(e.g., TATARSKII, 1961; DOVIAK and ZRNIĆ, 1984), where $G(\mathbf{x}')$ is a complex-valued instrument function, or "sampling function" that does not vary with time. DOVIAK and ZRNIĆ (1984) put forward a closed-form model for $G(\mathbf{x}')$ which is a good approximation for a wide range of RWP applications.

While DOVIAK and ZRNIĆ (1984), and recently MUSCHINSKI (2004), discuss the power

$$P_r = \frac{R}{2}\langle |I|^2 \rangle \tag{2.7}$$

of the backscattered pulse measured at the receiver output (here R is the receiver resistance) by means of Eq. (2.6), the traditional approach by TATARSKII (1961) is slightly different. TATARSKII (1961, chapter 4) considered the electric field vector associated with a plane wave travelling through a small test volume V and used Maxwell's equations to find the field vector of the wave scattered into a particular direction $\mathbf{m}$ (TATARSKII, 1961, p. 63, eq. 4.8). Then he derived the mean intensity of the scattered wave and derived an equation for the scattering cross-section increment $d\sigma$ for the wave scattered from the scattering volume V into a solid-angle increment $d\Omega$ in the direction $\mathbf{m}$:

$$d\sigma = 2\pi k_0^4 V \sin^2\chi \Phi_{nn}(\mathbf{k}_0 - k_0\mathbf{m})\, d\Omega \tag{2.8}$$

(TATARSKII, 1961, p. 68, eq. 4.19), where $k_0 = 2\pi/\lambda$ is the wave number of both the incident wave and the scattered wave, χ is the angle between the elctromagnetic field vector of the incident wave and the propagation direction $\mathbf{m}$ of the scattered wave, $\mathbf{k}_0$ is the wave vector of the incident wave, $\mathbf{m}$ is the wave vector of the scattered wave, and $\Phi_{nn}(\mathbf{k})$ is the three-dimensional, spectral density of refractive-index variance at the wave vector $\mathbf{k}$. For backscatter, we have $\chi = 90^o$ (the field vector is perpendicular to the propagation path) and $\mathbf{k}_0 - k_0\mathbf{m} = 2\mathbf{k}_0$. The magnitude of the "Bragg wave vector" $2\mathbf{k}_0$ is usually referred to as the Bragg wave number,

$$k_B = 2k_0 = \frac{4\pi}{\lambda}. \tag{2.9}$$

If the refractive-index perturbations are statistically isotropic at a particular wave number k, and if k lies within the inertial subrange of the refractive-index turbulence, both of which are common, although not unchallenged assumptions for atmospheric refractive-index perturbations at wavelengths of 1 m or shorter (e.g., MUSCHINSKI and WODE, 1998; LUCE et al., 2001a; MUSCHINSKI and LENSCHOW, 2001; BALSLEY et al., 2003), then $\Phi_{nn}(\mathbf{k})$ depends only on the magnitude k of the wave vector and is proportional to the refractive-index structure parameter C_n^2:

$$\Phi_{nn}(\mathbf{k}) = \frac{\Gamma(8/3)\sin(\pi/3)}{4\pi^2} C_n^2 k^{-11/3} = 0.0330\, C_n^2 k^{-11/3} \tag{2.10}$$

(TATARSKII, 1961, p. 48, eq. 3.24).

It has become common practice to quantify the ratio between incident and backscattered intensity in terms of the volume reflectivity

$$\eta = \frac{1}{V} \frac{d\sigma_b}{d\Omega/4\pi}, \tag{2.11}$$

where $d\sigma_b$ is the cross-section increment for backscatter, i.e., $\chi = 90^o$ and $\mathbf{k}_0 - k_0\mathbf{m} = 2\mathbf{k}_0$. Inserting (2.8) leads to

$$\eta = 8\pi^2 k_0^4 \Phi_{nn}(2\mathbf{k}_0). \tag{2.12}$$

If the volume V is filled with refractive-index turbulence that is isotropic at the Bragg wave number and homogeneous across the volume V, and if $2k_0$ lies in the inertial subrange, then (2.10) is valid and one obtains

$$\eta = 0.379\, C_n^2 \lambda^{-1/3}. \tag{2.13}$$

This relationship follows immediately from Tatarskii's analysis, as just shown, but is usually credited to OTTERSTEN (1969) who, to the best of our knowledge, was the first to present the relationship between η and C_n^2 in the form of Eq. (2.13).

The advantage of the DOVIAK and ZRNIĆ (1984) approach is that it avoids the concept of a local scattering cross section, which may cause problems if the refractive-index correlation lengths are not small compared to the Fresnel length. This was recently pointed out by TATARSKII (2003), who now strongly questions his earlier approach. MUSCHINSKI (2004), however, found that both approaches, that is, the Fraunhofer approximation (TATARSKII, 1961) and the Fresnel approximation (DOVIAK and ZRNIĆ, 1984), lead to the same result, namely to Eq. (2.13), if the refractive-index perturbations are Bragg-isotropic, which in many cases is a valid assumption, in particular for UHF RWPs operating in the atmospheric boundary layer.

2.5 Combining radio-wave propagation theory with basic fluid dynamics: The relationship between Doppler shift and radial wind velocity

The main purpose of a radar wind profiler is to measure vertical profiles of the three components, u, v, and w, of the wind vector. The standard procedure is the so-called Doppler beam swinging (DBS) technique, where the radial wind velocity, v_r, is measured in at least three non-coplanar beam directions, and u, v, and w are retrieved from the v_r measurements by means of elementary trigonometric relationships. For a given beam direction, v_r is obtained through

$$\omega_D = -k_B v_r, \tag{2.14}$$

where

$$\omega_D = \frac{\int \phi(\omega)\,\omega\, d\omega}{\int \phi(\omega)\; d\omega} \tag{2.15}$$

is the Doppler shift. In the measurement example discussed in Section 2, the radar wavelength was 62 cm and the Doppler shift was -18 Hz, such that $v_r = +5.6$ m s^{-1}. A negative Doppler shift and a positive v_r means that the air moves away from the radar.

For more than two decades, the v_r-ω_D relationship, (2.14), has been the key equation for operational RWP. Eq. (2.14) can be derived easily based on the assumption that the scattering volume is populated by point scatterers that are advected with the wind velocity. In the case of scatter from turbulence, however, which is the usual case for RWP applications, there are no point scatterers. Instead, the scattering volume is filled with a continuous refractive-index field that is random in time and space and is usually characterized by horizontal correlation lengths that are large compared to the size of the scattering volume and by correlation times that are long compared to the dwell time.

Although it is obvious that the point-scatterers assumption is invalid for most RWP applications, for more than two decades, the RWP community has taken the validity of (2.14) for granted. Doubts that (2.14) might be incomplete or erroneous have come from different sources. HOCKING et al. (1986) showed that Bragg-anisotropy, which is common for echoes observed with VHF radars at near-zenith directions and is known as “VHF aspect sensitivity,” leads to erroneous radial wind velocities, and they suggested a correction formula. NASTROM and VANZANDT (1994) found that long-term averages of vertical velocities observed with vertically pointing VHF radars usually show a downward bias of a few centimeters per second, and they explained this bias with a negative covariance between vertical-velocity fluctuations and radar-reflectivity fluctuations resulting from upward-propagating gravity waves. MUSCHINSKI (1996) offered an alternative explanation: Bragg-anisotropic features associated with Kelvin-Helmholtz billows in the shear regions of upper-level jet streams lead to a downward bias in the lower shear region and an upward bias in the upper shear region. Recently, the upward bias hypothesized by MUSCHINSKI (1996) was observed by YAMAMOTO et al. (2003).

To the best of our knowledge, MUSCHINSKI (1998) was the first to use the basic equation for single scatter, (2.6), to investigate the validity of the traditional v_r-ω_D relationship (2.14) for the case of scatter from turbulent refractive-index perturbations advected by a turbulent wind field. He found that in general, ω_D is the sum of three parts: first, the mean-wind contribution, $-k_B v_r$, which is the only term that appears in the traditional v_r-ω_D relationship (2.14); second, a term that is proportional to the Bragg-component of the spatial quadrature spectrum of radial-wind and refractive-index perturbations, a term that TATARSKII and MUSCHINSKI (2001) later called the “correlation velocity;” and a third term that is proportional to the covariance of v_r perturbations and η perturbations, or, in other words, proportional to the radial flux of clear-air radar reflectivity.

Recently, MUSCHINSKI (2004) expanded and generalized the earlier analysis (MUSCHINSKI, 1998) and found for the mth moment of the Doppler spectrum, $M_{11}^{(m)}$, the equation

$$M_{11}^{(m)} = \frac{1}{i^m} \iiint \iiint G_{11}\left(\mathbf{x}',\mathbf{x}''\right) R_{nn}^{(m)}\left(\mathbf{x}',\mathbf{x}''\right) d^3x' d^3x'', \tag{2.16}$$

where

$$R_{nn}^{(m)}\left(\mathbf{x}',\mathbf{x}''\right) = \left\langle n\left(\mathbf{x}'\right) \frac{\partial^m}{\partial t^m} n\left(\mathbf{x}''\right) \right\rangle \tag{2.17}$$

is the two-point, cross-covariance function of the refractive index and of the mth local time derivative of the refractive index, and where

$$G_{11}\left(\mathbf{x}',\mathbf{x}''\right) = G_1^*(\mathbf{x}')G_1(\mathbf{x}'') \tag{2.18}$$

is a new instrument function.

MUSCHINSKI (2004) studied $R_{nn}^{(1)}\left(\mathbf{x}',\mathbf{x}''\right)$ and $R_{nn}^{(2)}\left(\mathbf{x}',\mathbf{x}''\right)$ based on simplifying assumptions like the random Taylor hypothesis. Much further work, however, needs to be done to systematically investigate the functions $R_{nn}^{(m)}\left(\mathbf{x}',\mathbf{x}''\right)$, which would be the basis of a full understanding of the higher moments of RWP Doppler spectra.

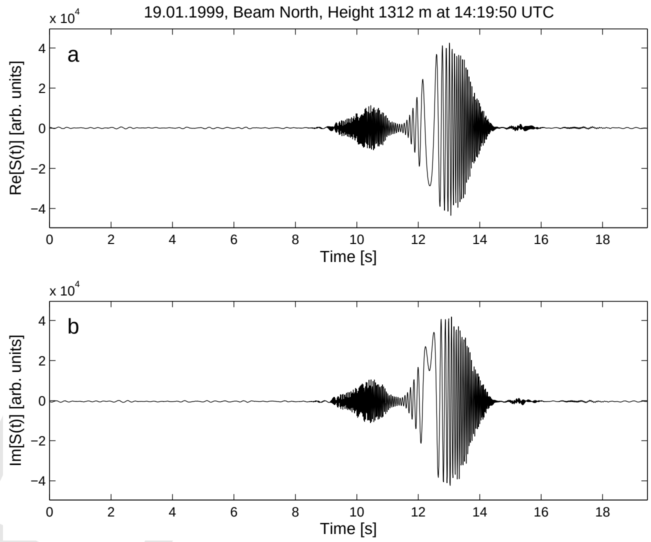

Figure 5: Time series of the in-phase (a) and quadrature (b) component of an RWP signal with severe aircraft echo contamination.

2.6 Non-stationary clutter and time-frequency decomposition

Aircraft, birds, and moving objects on the ground may severely contaminate RWP signals. Often their echo intensity exceeds the clear-air echo intensity by several orders of magnitude, and their radial velocities may vary from centimeters per second to tens (birds, cars) or even hundreds of meters per second. An important feature of this type of clutter is that its Doppler frequency may change significantly during the dwell time. As we will see, these so-called transient or non-stationary signals can be resolved sufficiently well neither in time domain nor in frequency domain.

An example of a signal that is severely contaminated by an aircraft echo is given in Figure 5. The *transient* airplane clutter between t = 9 s and t = 16 s is much stronger than the clear-air echoes, which are not resolved in the figure. This contamination shows a typical variation in amplitude with distinct maxima and minima. This amplitude variation is a direct result of the antenna radiation pattern of the RWP. A calculated pattern for the Lindenberg 482-MHz RWP is shown in Figure 6. Assume that a hard target with constant radar reflectivity is moving through the RWP antenna beam. It will necessarily experience a varying illumination which in turn will lead to a varying echo amplitude. The observed amplitude modulation will therefore depend on the real radiation pattern of the antenna, the flight trajectory, and the speed of this target. A simple theoretical model for an airplane return was given by BOISSE et al. (1999).

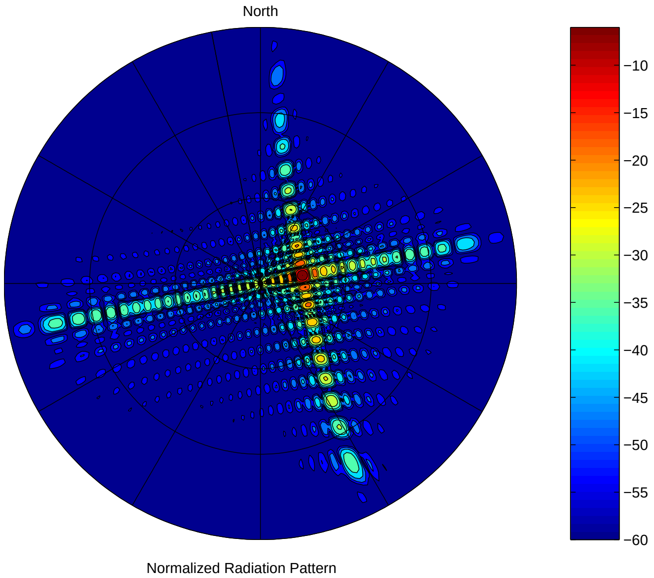

Figure 6: Ideal antenna radiation pattern of the east beam of the Lindenberg 482 MHz RWP.

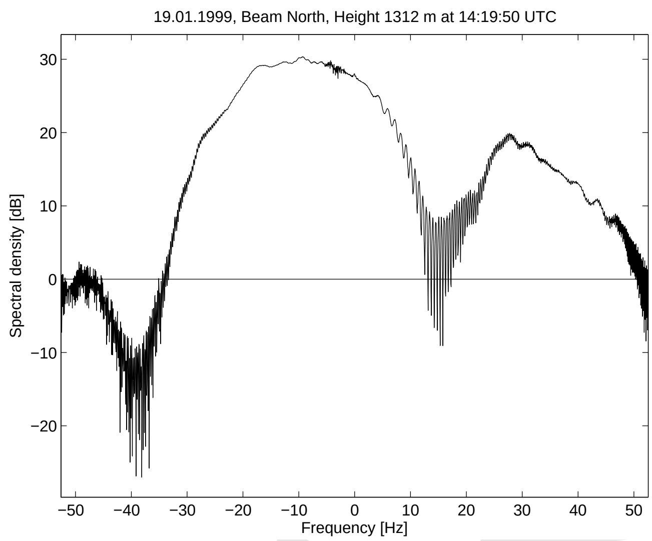

Figure 7: Frequency spectrum of the signal shown in Figure 5.

The frequency spectrum of the contaminated signal is depicted in Figure 5. Because of the transient nature of the aircraft echo, the clutter signal occupies a fairly wide frequency range, and it is nearly impossible to identify the clear-air component in the spectrum. The noise level at 0 dB computed with the algorithm by HILDEBRAND and SEKHON (1974) does not make much sense here, since noise is completely dominated by the airplane echo. It is obvious that neither the time series nor the spectrum is an adequate representation to characterize the properties of this signal.

Generally, time representation (sampled data) and frequency representation (Fourier transformed signal) are two alternative ways of looking at the same piece of information. The time representation offers the highest resolution in time, but there is no frequency resolution. That means two signal components can still be distinguished even if their energy is concentrated within a very short, but non-overlapping period of time, no matter what frequency information the two components carry. On the other hand, if two components overlap in time, they cannot be distinguished, even if their energy is concentrated at different frequencies. Also, it is difficult to read the desired frequency information from a pure time-domain representation.

Frequency representation possesses the highest possible frequency resolution, but there is no time resolution. For transient signals such as airplane echoes, neither representation is optimal, as we will see in the following example.

We construct a simple test signal consisting of two components: A (stationary) harmonic wave $s_1(t)$ and a (non-stationary) damped linear chirp $s_2(t)$ are added to yield the two-component signal $s(t)$:

$$
\begin{aligned}
s(t) &= s_1(t) + s_2(t) \\
&= \exp(2\pi i f_0 t) \\
&\quad +100 \exp\left(-\frac{t^2}{2\sigma^2}\right) \exp\left(2\pi i \cdot \frac{1}{2} a t^2\right),
\end{aligned}
\tag{2.19}
$$

where we choose the constant frequency $f_0 = 3$ Hz, the angular acceleration a = 0.6 Hzs^{-1} and the damping factor $\sigma = 5$ s. The signal s and its Fourier spectrum are shown in Figures 8 and 9, respectively. Since s_2 exceeds s_1 by two orders of magnitude, s_1 is no longer visible in the time series plot. In the frequency spectrum, s_1 is observed as a small kink at $f_0 = 3$ Hz. The instantaneous frequency of an analytic signal $s(t) = A(t)\exp[i\Phi(t)]$ is defined as $f_{\text{inst}}(t) = \frac{1}{2\pi}\frac{d}{dt}[\Phi]$ (HLAWATSCH and BOUDREAUX-BARTELS, 1992; BOASHASH, 1992; FLANDRIN, 1999). For the non-stationary component s_2, we obtain $f_{\text{inst}}(t) = \frac{d}{dt}(\frac{1}{2}at^2) = at$. Because the instantaneous frequency changes in time, the signal energy is spread over the whole axis in both time and frequency domain. In neither time, nor frequency representation, s_1 and s_2 can be separated easily.

A better way to facilitate the understanding of such signals is provided by so-called time-frequency (TF) representations. The most prominent TF representations are linear, like the short-time or windowed Fourier transform (WFT) or wavelet transforms.[1]. Other TF representations are quadratic, such as the spectrogram, the scalogram or the Wigner-Ville distribution (COHEN, 1989; HLAWATSCH and BOUDREAUX-BARTELS, 1992; FLANDRIN, 1999).

Time-frequency representations are yet another way of looking at a signal; they are a compromise between

[1]Wavelet transforms are usually referred to as a time-scale representation, where scale is the reciprocal of frequency.

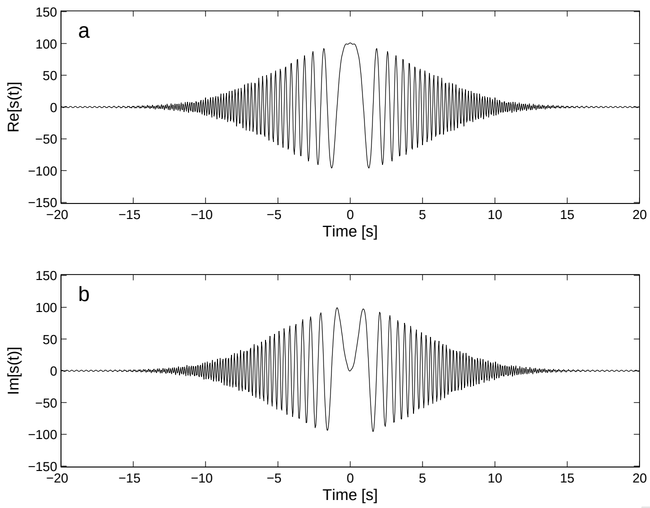

Figure 8: In-phase (a) and quadrature (b) component of test signal *s*.

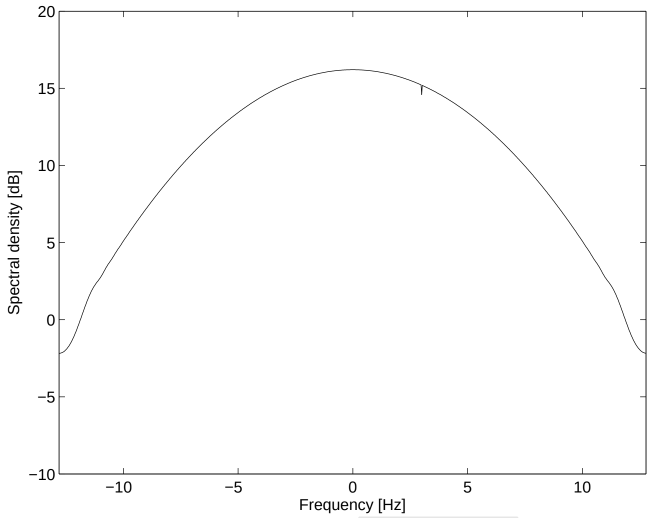

Figure 9: Frequency spectrum of the test signal *s*.

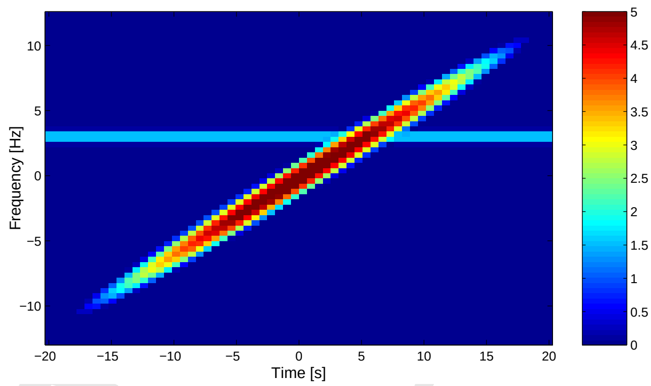

Figure 10: Spectrogram of the test signal *s*.

time and frequency representation. If properly chosen, linear TF representations contain exactly the same amount of information, and the original signal can be stably reconstructed. Here we will concentrate on the WFT having these properties. Other successful attempts using wavelet methods for filtering RWP signals have already been made (JORDAN et al., 1997; BOISSE et al., 1999; LEHMANN and TESCHKE, 2001; JUSTEN et al., 2004).

The WFT maps an univariate signal $s(t)$ to a bivariate function $F_s(t,f)$. Time resolution can be traded for frequency resolution but both resolutions cannot be made arbitrarily high at the same time. The WFT using a Gaussian window function offers optimal time-frequency resolutions (GABOR, 1946; MALLAT, 1999). Thus, we will use this type of window.

Figure 10 shows a spectrogram of the signal *s* in (2.19). A spectrogram is defined as the squared absolute value of the WFT $F_s(t,f)$. This gives — similarly to the Fourier spectrum — a measure of signal energy. The stationary part s_1 appears as a horizontal line at $f_0 = 3$ Hz. The non-stationary part s_2 is visible as an inclined line with slope a = 0.6 Hzs^{-1}. Note that the overlap of s_1 and s_2 is rather small. Thus, both parts can now be easily separated.

The airplane echo shown in the beginning of this Section has a structure similar to the transient signal s_2. Thus, we exemplarily show how it is possible to remove s_2, while at the same time keeping the stationary part s_1. Figure 11 schematically explains our method. For fixed $\bar{f}$, one "row" $F_s(\cdot,\bar{f})$ shows a large peak at a time where the instantaneous frequency $f_{\text{inst}}(t) = at$ of the transient component s_2 meets $\bar{f}$. However, the stationary part s_1 does not produce such a peak since it does not change frequency in time. When $\bar{f}$ happens to match the frequency f_0 of s_1, the overall level of $F_s(\cdot,\bar{f})$ will be larger, but there will be no peak. Hence, by removing the peaks in every row of the WFT and setting the corresponding coefficients to zero, we completely remove the transient part. The stationary part is left almost unaffected. Only small parts of s_1 are removed, namely, where s_1 and s_2 overlap. Note that for clarity, Figure 11 only shows the real part of the spectrogram. The actual filtering is carried out on the complex WFT.

A filtered signal can now be reconstructed from the filtered WFT. Figures 12 and 13 show the filtered signal and its Fourier spectrum. The filtered signal clearly resembles the sinusoidal wave s_1 up to a certain neighborhood of $t = f_0/a = 5$ s, where some parts have been accidentally removed. In the Fourier spectrum, we see a peak at $f_0 = 3$ Hz. Nothing is left from the non-stationary component s_2.

We will now apply these ideas to the contaminated signal given in Figure 5. Figure 14 shows a spectrogram of this signal. Due to their stationary nature, ground clutter and clear-air signal appear as *horizontal* lines at 0 Hz and -4 Hz, respectively. A strong airplane echo emerges as *diagonal* lines from $t = 6$ s to $t = 18$ s. The more pronounced falling diagonal is the actual airplane echo. Its slope is directly related to the *change* of radial velocity of the airplane (BOISSE et al., 1999), which is significant in the measurement period. The crossing of different radar antenna side lobes results in an oscillatory amplitude behaviour. The falling diagonal is aliased at $t = 9$ s and $t = 16$ s.

The raising diagonal, which is an attenuated and mirrored version of the falling one, is an echo phantom (the so-called "mirror image") resulting from imperfect quadrature of I and Q in the receiver (DOVIAK and ZRNIĆ, 1993).

In Figures 15 to 17, the filtered spectrogram, the filtered signal and the filtered Fourier spectrum are presented. The strong airplane echo from $t = 9$ s to $t = 16$ s (compare Figure 5) has vanished. The clear-air signal, which could only be observed as a small oscillation at -4 Hz in the unfiltered spectrum, now dominates the Fourier spectrum. A smaller ground-clutter peak has also been revealed.

It is especially remarkable that the method performs so well even though the signal-to-clutter ratio (computed from the original and filtered spectrum) is -32 dB, which is a result of the TF representation's ability to separate transient and stationary components. This is closely related to its time-frequency resolution, which is optimal for the WFT using a Gaussian window. Thus, this method is particularly suitable for intermittent clutter filtering.

Note that in contrast to intermittent clutter, both ground clutter and the clear-air signal are stationary. Therefore, it does not seem to make sense to address the problem of ground clutter filtering with time-frequency methods. Fourier methods seem to be more appropriate here.

3 Two-signal radar wind profiling

In the previous section, we described several aspects of a single signal measured with an RWP. Modern RWP, however, offers the possibility to sample the same scattering volume with different sampling functions at the same time. In this section, we consider the additional information that can be extracted from the *cross-covariance function* and the *cross-spectrum* of *two* signals,

$$I_1(t) = \iiint G_1(\mathbf{x}')\, n(\mathbf{x}',t)\, dx' \tag{3.1}$$

and

$$I_2(t) = \iiint G_2(\mathbf{x}'')\, n(\mathbf{x}'',t)\, dx'', \tag{3.2}$$

where $G_1(\mathbf{x}')$ and $G_2(\mathbf{x}'')$ are two different sampling functions that overlap in space in some well-defined and well-designed fashion. Before we discuss properties of and design criteria for the sampling functions in more detail, we consider the cross-covariance function

$$C_{12}(t,\tau) = \langle I_1^*(t)\, I_2(t+\tau)\rangle\,. \tag{3.3}$$

Here, the angular brackets stand for the ensemble average.

3.1 Cross-covariance function and cross-spectrum of two RWP signals

In general, $C_{12}(t,\tau)$ is a function of both time t and time lag τ. For many RWP applications, however, it is a valid assumption that $I_1(t)$ and $I_1(t)$ are statistically stationary during the dwell time, such that C_{12} is a function only of τ. Then we have

$$C_{12}(\tau) = \iiint \iiint G_{12}(\mathbf{x}',\mathbf{x}'')\, R_{nn}^{(0)}(\mathbf{x}',\mathbf{x}'',\tau)\, d^3x' d^3x'', \tag{3.4}$$

where

$$G_{12}(\mathbf{x}',\mathbf{x}'') = G_1^*(\mathbf{x}')\, G_2(\mathbf{x}'') \tag{3.5}$$

is the combined sampling function and

$$R_{nn}^{(0)}(\mathbf{x}',\mathbf{x}'',\tau) = \langle n(\mathbf{x}',t)\, n(\mathbf{x}'',t+\tau)\rangle \tag{3.6}$$

is the spatial autocovariance function of the refractive index.

In full analogy to the definition of the Doppler spectrum in the single-signal case, we now define the Doppler cross-spectrum for the two-signal case:

$$\phi_{12}(\omega) = \frac{1}{2\pi}\int C_{12}(\tau)\exp(-i\omega\tau)\, d\tau. \tag{3.7}$$

As in the single-signal case, the lowest spectral moments are of particular interest. The mth cross-spectral moment is

$$M_{12}^{(m)} = \int \phi_{12}(\omega)\, \omega^m d\omega. \tag{3.8}$$

According to the moments theorem — a derivation for complex-valued signals can be found in Appendix A of MUSCHINSKI (2004) —, the mth moment is (apart from the phase factor i^m) equal to the mth τ-derivatives of $C_{12}(\tau)$ at zero time lag:

$$M_{12}^{(m)} = \frac{1}{i^m}\frac{\partial^m}{\partial\tau^m} C_{12}(\tau)\bigg|_{\tau=0}. \tag{3.9}$$

It is straightforward (MUSCHINSKI, 2004) to express the spectral moments in terms of $G_{12}(\mathbf{x}',\mathbf{x}'')$ and $R_{nn}^{(m)}(\mathbf{x}',\mathbf{x}'')$:

$$M_{12}^{(m)} = \frac{1}{i^m}\iiint\iiint G_{12}(\mathbf{x}',\mathbf{x}'')\, R_{nn}^{(m)}(\mathbf{x}',\mathbf{x}'')\, dx' dx'', \tag{3.10}$$

where $R_{nn}^{(m)}(\mathbf{x}',\mathbf{x}'')$ is the spatial cross-covariance function of the refractive index and the mth local time derivative of the refractive index, as introduced in Section 2.5. Note that all spectral moments are unambiguously described by a *purely spatial* refractive-index statistic.

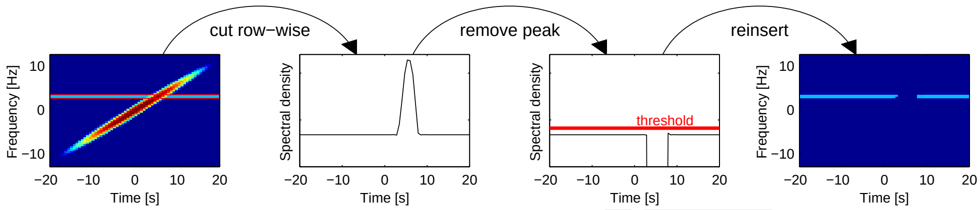

Figure 11: Filtering process. Transient signal components induce peaks in rows of the spectrogram (second from left). They are removed by a thresholding process (second from right), where the threshold is automatically selected from each row. The filtered spectrogram (right) or rather the filtered WFT is reconstructed to a filtered time series.

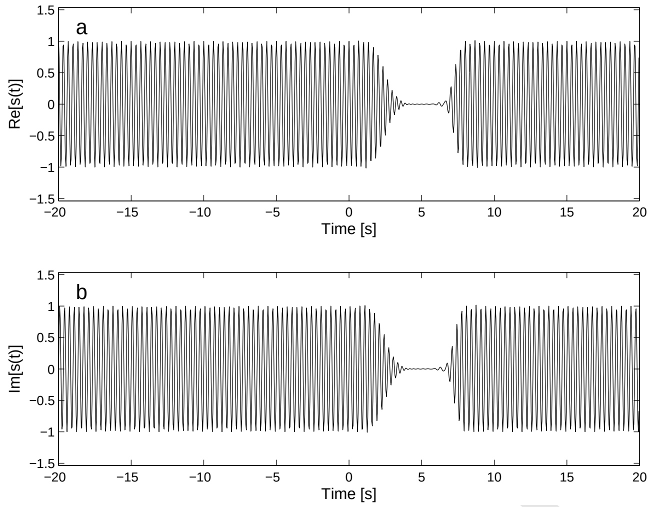

Figure 12: Filtered signal, reconstructed from the filtered WFT (see Figure 11).

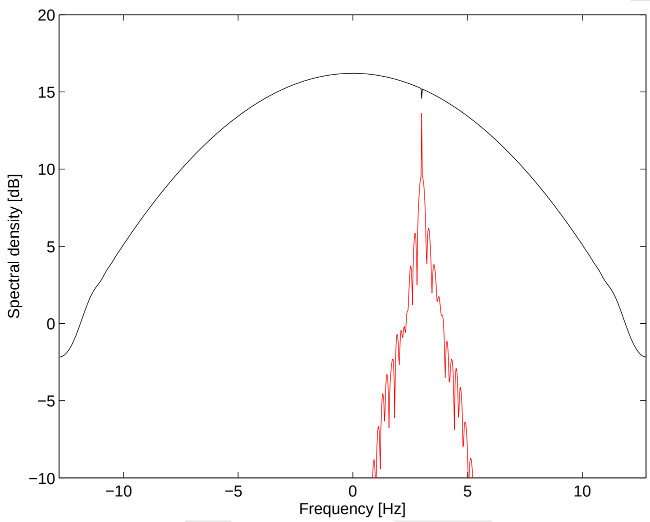

Figure 13: Fourier spectrum of the original signal *s* (black) and spectrum of the corresponding filtered signal (red).

3.2 Two-signal RWP techniques

The general equation (3.10) can now be applied to various families of instrument functions $G_{12}(\mathbf{x}', \mathbf{x}'')$. These families are associated with different "two-signal RWP techniques". The different $G_{12}(\mathbf{x}', \mathbf{x}'')$ families are distinguished by how the two sampling functions $G_1(\mathbf{x}')$

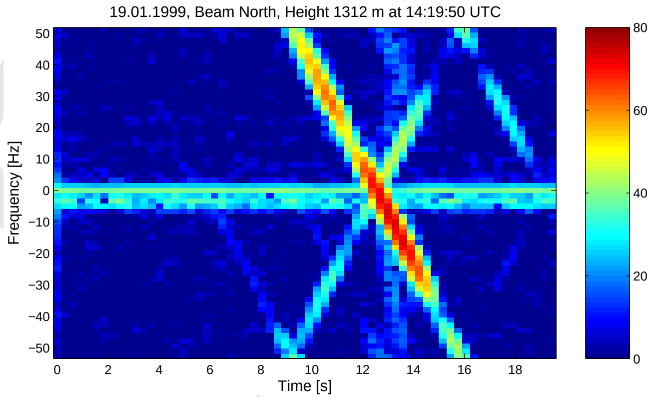

Figure 14: Spectrogram of the signal shown in Figure 5.

and $G_2(\mathbf{x}'')$ differ from each other. The two techniques that so far have been used most often are the frequency-domain interferometry (FDI) and the spaced-antenna (SA) technique, which we describe first. Later, we discuss the outlook for using other possibilities to take advantage of two-signal RWP.

FDI was first implemented by KUDEKI and STITT (1987) at the Jicamarca VHF radar. The idea is to sample the same scattering volume simultaneously and phase-coherently with two (slighty) different Bragg wavelengths. This requires operating the radar with two different carrier frequencies, f_1 and f_2. FDI enables one to retrieve two parameters that cannot be measured with single-signal RWP: the radial location of a (single) localized scatterer (or scattering layer) within the pulse volume and the radial extent, or thickness, of the scatterer or scattering layer. While the phase of the (complex) signal covariance $C_{12}(\tau = 0)$ provides the location, the magnitude of $C_{12}(\tau = 0)$ gives the thickness.

FDI has been successfully used to observe the structure and evolution of features whose height extent is small compared to the radar's pulse length. CHILSON et al. (1997) were the first to use FDI to track upper-tropospheric Kelvin-Helmholtz billows with a height resolution of about twenty meters, although the pulse length, which defines the range resolution for single-signal RWP, was as large as 300 m. MUSCHINSKI et al. (1999) were the first to apply FDI for the observation of the slow downward motion of long-lived layers in the free troposphere. In general, the local temporal rate of change of layer height is dominated by the horizontal advection of a tilted layer. But in a time-height window where the horizontal wind speed was very small, MUSCHINSKI et al. (1999) retrieved the same downward velocity of 2 $\mathrm{cm\,s^{-1}}$ from three independent sources: the temporal change of FDI-retrieved layer height, the single-signal Doppler shifts, and the vertical motion diagnosed with a regional weather forecasting model. The magnitude and sign of that small vertical velocity was consistent with the subsidence associated with the high-pressure area that characterized the lower troposphere above the radar site at the observation time. Both the CHILSON et al. (1997) study and the MUSCHINSKI et al. (1999) study were carried out in the Harz Mountains in Northern Germany, using the SOUSY VHF radar operated by the Max-Planck Institut für Aeronomie in Katlenburg-Lindau. (SOUSY stands for “Sounding System”.)

The SA technique takes advantage of the possibility to observe the backscattered echo simultaneously with different receiving antennas (e.g., DOVIAK et al., 1996). For typical SA applications, the beam axes of the transmitting antenna and of the various receiving antennas are all vertical. Two signals I_1 and I_2 measured with receiving antennas R1 and R2 are highly correlated if the (horizontal) spacing between R1 and R2 is small. In the limit of zero spacing, R1 and R2 are identical, such that $I_1 = I_2$, and the problem reduces to the single-signal case. The correlation decreases rapidly with increasing spacing. There is an optimum spacing, for which the energy in the imaginary part of $\phi_{12}(\omega)$, i.e., in the quadrature spectrum, reaches a maximum. While the normalized first moment of the co-spectrum (i.e., the real part of $\phi_{12}(\omega)$), provides the vertical velocity, the first normalized moment of the quadrature spectrum gives the “baseline wind,” i.e., the component of the wind velocity vector along the direction of the horizontal spacing vector between R1 and R2. According to the moments theorem, the first moment of the quadrature spectrum is (apart from the factor i) identical to the slope of the imaginary part of $C_{12}(\tau)$ at $\tau = 0$. It is not clear why practically all researchers using the SA technique retrieve the baseline winds from $C_{12}(\tau)$ (e.g., LATAITIS et al., 1995) and not from $\phi_{12}(\omega)$.

The SA technique has various advantages and disadvantages as compared to the widely used DBS technique. The two main advantages of the SA technique are the possibility to retrieve all three wind components from the same scattering volume, which makes SA less sensitive to errors induced by small-scale, horizontal inhomogeneity of the vertical wind (such inhomogeneity is known to severely affect DBS wind measurements; see, e.g., WEBER et al., 1992), and the lack of the need to use off-zenith beam directions. Disadvantages include the need to receive multiple signals simultaneously, the smaller signal-to-noise ratio, and the higher vulnerability to fading ground clutter. No consensus has yet been reached in the RWP community as to whether the DBS or the SA technique is to be preferred for operational purposes.

Other, more exotic two-signal RWP techniques are conceivable: sampling the same scattering volume with two different pulse lengths and/or receiver bandwidths; sampling the same volume simultaneously with two slightly different beam directions; or sampling the same volume simultaneously with two different beamwidths. It seems that none of these possibilities has been thoroughly explored so far.

4 Multi-signal radar wind profiling

As a generalization of single-signal or two-signal wind profiling, meteorological information can be extracted from the covariance matrix or the cross-spectral moment matrix of multiple signals S_j, $j = 1, \ldots, J$, which characterize the same scattering volume during the same time. It is important that the J signals are sampled phase-coherently and with a sampling period that is short compared to the correlation time of the clear-air component. There are various radar parameters with respect to which these signals may be different from each other but still represent structure and dynamics in the same volume of air. These parameters include the carrier frequency, the location of the receiving antenna, the center of the range gate, and the pulse length.

4.1 Optimization of the sampling function

For a monostatic radar, the sampling function $G(\mathbf{x})$ in the far field is given by

$$G(\mathbf{x}) = A(\mathbf{x}) \exp\left[-i\beta\left|-\mathbf{r}_0 + \mathbf{x}\right|\right] \tag{4.1}$$

(DOVIAK and ZRNIĆ, 1984; MUSCHINSKI, 2004), where $A(\mathbf{x})$ is a three-dimensional amplitude weighting function that defines the sampling volume, β is the Bragg wavenumber, $\mathbf{r}_0$ is the vector pointing from the center of the sampling volume to the antenna center, and $\mathbf{x}$ is the location relative to the center of the sampling volume.

Now, assume that a set of J phase-coherent signals

$$I_j(t) = \iiint G_j\left(\mathbf{x}'\right) n\left(\mathbf{x}', t\right) d^3x', \tag{4.2}$$

is available, where we assume that in general the $G_j(\mathbf{x}')$ differ from each other only with respect to the Bragg wavenumber β_j, the three-dimensional envelope of the pulse, and the range:

$$G_j\left(\mathbf{x}'\right) = A_j\left(\mathbf{x}'\right) \exp\left[-i\beta_j\left|-\mathbf{r}_j + \mathbf{x}'\right|\right]. \tag{4.3}$$

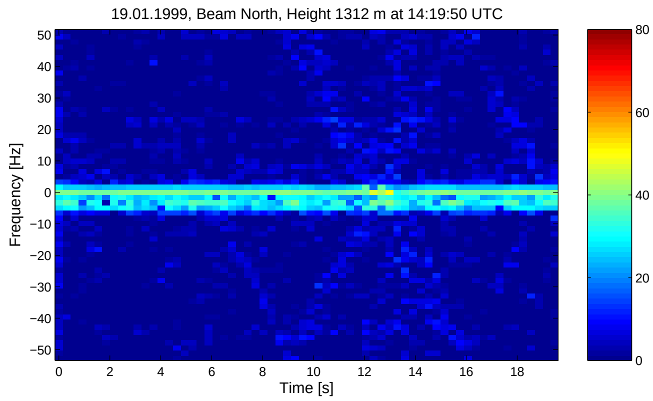

Figure 15: Spectrogram after removal of the aircraft clutter.

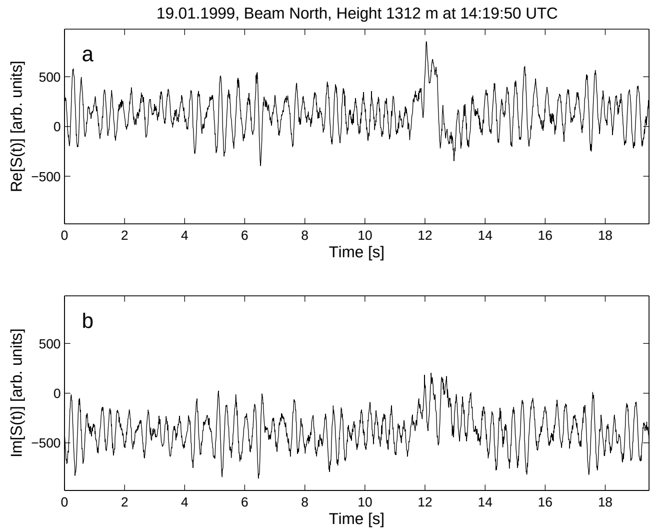

Figure 16: Signal, reconstructed from the filtered WFT (spectrogram shown in Figure 15).

For complex-valued weight coefficients w_j $(j = 1, \ldots, J)$ we may consider the "synthesized" signal

$$I(t) = \sum_{j=1}^{J} w_j I_j(t), \tag{4.4}$$

which can be written in the same form as the integral for $I_j(t)$,

$$I(t) = \iiint G(\mathbf{x}')\, n(\mathbf{x}', t)\, d^3x', \tag{4.5}$$

where

$$G(\mathbf{x}') = \sum_{j=1}^{J} w_j G_j(\mathbf{x}').$$

Here we assume that the refractive-index perturbations at a fixed location $\mathbf{x}$ are statistically stationary with respect to time. Note that $I(t)$ is of the same form as in the standard case, except that now the instrument function $G(\mathbf{x}')$ can be some arbitrary function in the linear span of $G_1, \ldots, G_J$ because there are *a priori* no constraints with respect to the weighting vector w_j. Moreover, there

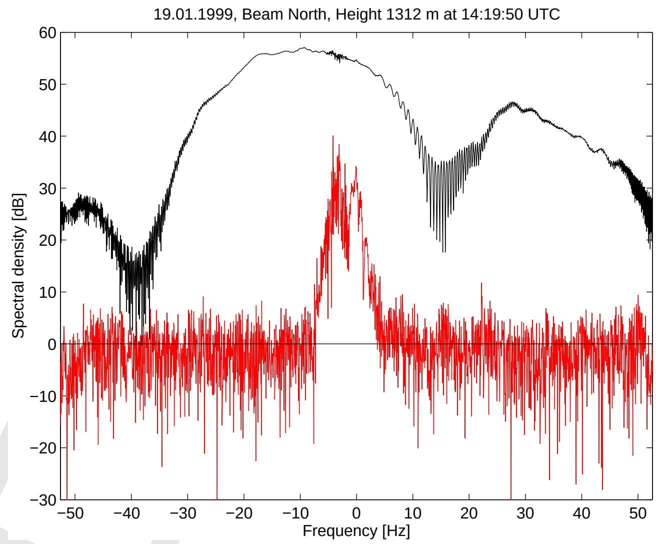

Figure 17: Fourier spectrum of the original RWP signal (black) shown in Figure 5 and spectrum of the corresponding filtered signal (red) from Figure 16.

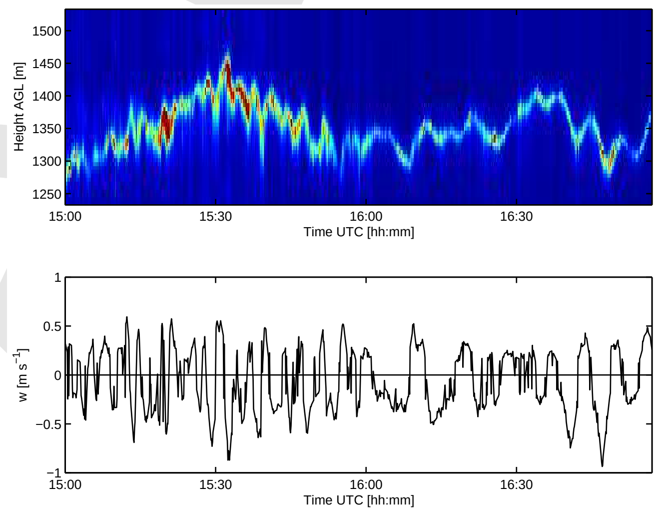

Figure 18: (a) Time-height cross section of "RIM brightness" retrieved from the first UHF RIM measurements. The data were collected on April 10, 2001, near Platteville, Colorado (Chilson et al., 2003). (b) Doppler velocities retrieved from the same raw data.

is nothing that would keep one from choosing w_j differently for different locations $\mathbf{x}$. Then we have

$$I(\mathbf{x}, t) = \sum_{j=1}^{J} w_j(\mathbf{x}) \iiint G_j(\mathbf{x}')\, n(\mathbf{x}', t)\, d^3x'. \tag{4.6}$$

That is, based on the finite set of J signals I_j that characterize a given scattering volume, we are now in the position to synthesize an infinite set of new signals $I(\mathbf{x}, t)$ by means of (4.6). Because $w_j(\mathbf{x})$ can be freely chosen, there is no constraint for the spatial variability of $I(\mathbf{x}, t)$ within the same scattering volume. The *general problem* is how to find the $w_j(\mathbf{x})$ that allows us to retrieve meteorological information with *maximum ac-*

curacy.

In order to attack this problem, we assume that the weight vector $\mathbf{w}(\mathbf{x}) = (w_1(\mathbf{x}),\ldots,w_J(\mathbf{x}))$ is complex valued; i.e. $w_j(\mathbf{x}) = W_j(\mathbf{x})\exp(i\varphi_j(\mathbf{x}))$, such that $W_j(\mathbf{x}) \in \mathbf{R}$ with $\sum_{j=1}^{J} W_j(\mathbf{x}) = 1$ point-wise for all $\mathbf{x}$. The main constraint for the weighting vector follows from the assumption that at $\mathbf{x}' = \mathbf{x}$, the components $w_j(\mathbf{x})G_j(\mathbf{x})$ shall constructively interfere. Here, $\mathbf{x}$ is the location "to be imaged." This leads (modulo a factor 2π) to

$$\begin{aligned}&\exp(i\varphi_j(\mathbf{x}))\exp[-i\beta_j|-\mathbf{r}_j+\mathbf{x}|] = 1,\\ &\text{or equivalently}\quad \varphi_j(\mathbf{x}) = \beta_j|-\mathbf{r}_j+\mathbf{x}|\end{aligned} \qquad (4.7)$$

for $j = 1,\ldots,J$. This results in the condition

$$\mathbf{e}^H(\mathbf{x})\mathbf{w}(\mathbf{x}) = 1, \qquad (4.8)$$

where $\mathbf{e}^H(\mathbf{x}) := (\mathbf{e}^*(\mathbf{x}))^T = (\exp[i\beta_1|-\mathbf{r}_1+\mathbf{x}|],\ldots,\exp[i\beta_J|-\mathbf{r}_J+\mathbf{x}|])$ is sometimes referred to as the steering vector. The remaining task is to determine, for any given $\mathbf{x}$, the optimum vector $\mathbf{w}(\mathbf{x})$. This is achieved by a "side-lobe minimization." This requires that for a given $\mathbf{x}$, the signal variance

$$M_0(\mathbf{x}) \equiv \left\langle |I(\mathbf{x})|^2 \right\rangle \qquad (4.9)$$

is to be minimized through variation of the $\mathbf{w}(\mathbf{x})$. $M_0(\mathbf{x})$ can be expressed as follows

$$M_0(\mathbf{x}) = \mathbf{w}^H(\mathbf{x})\Psi\mathbf{w}(\mathbf{x}). \qquad (4.10)$$

The entries of the signal covariance matrix Ψ are given by

$$(\Psi)_{jk} = \langle I_j^* I_k \rangle. \qquad (4.11)$$

Combining the minimization of (4.9) and condition (4.8), we obtain the following optimization problem

$$\mathbf{w}^H(\mathbf{x})\Psi\mathbf{w}(\mathbf{x}) \to \min_{\mathbf{w}(\mathbf{x})},\quad \mathbf{e}^H(\mathbf{x})\mathbf{w}(\mathbf{x}) = 1. \qquad (4.12)$$

Since the problem is convex, there exists a minimizer which is given by

$$\mathbf{w}(\mathbf{x}) = \frac{\lambda}{2}\Psi^{-1}\mathbf{e}(\mathbf{x}) \qquad (4.13)$$

for some Lagrangian parameter λ. For computational details we refer the reader to the abundant literature, e.g., JUNGNICKEL (1999). In order to fulfill the constraint $\mathbf{e}^H(\mathbf{x})\mathbf{w}(\mathbf{x}) = 1$, the parameter λ must satisfy

$$\lambda = \frac{2}{\mathbf{e}^H(\mathbf{x})\Psi^{-1}\mathbf{e}(\mathbf{x})} \qquad (4.14)$$

and thus, combining (4.13) and (4.14), the optimal weight vector (and therewith the optimal G) is of the form

$$\mathbf{w}(\mathbf{x}) = \frac{\Psi^{-1}\mathbf{e}(\mathbf{x})}{\mathbf{e}^H(\mathbf{x})\Psi^{-1}\mathbf{e}(\mathbf{x})}. \qquad (4.15)$$

This is often referred to as the Capon-method.

4.2 Range imaging and coherent radar imaging as examples of multi-signal RWP

Motivated by the success of frequency-domain interferometry (FDI) in resolving thin scattering layers, and based on reasoning similar to what we have described in Section 4.1, PALMER et al. (1999) introduced range imaging (RIM), the multi-signal counterpart of FDI, which is a two-signal RWP technique. The underlying assumption of FDI is that there is only one scattering layer in a given resolution volume. RIM does not require that assumption to be fulfilled.

The first RIM observations were obtained with the SOUSY VHF radar during a five-day-long demonstration experiment in May 1999 (CHILSON et al., 2001; PALMER et al., 2001; MUSCHINSKI et al., 2001). Independently, on the Japanese MU radar LUCE et al. (2001b) implemented a technique that they called "frequency domain radar interferometric imaging" (FII). As explained in detail by MUSCHINSKI et al. (2001, p. 425), LUCE et al. (2001b) did not cycle fast enough through all frequencies and therefore could not fully exploit range-imaging capabilities. In other words, FII as implemented by LUCE et al. (2001b) is a hybrid of FDI and RIM.

The first RIM implementation on a UHF profiler was accomplished by CHILSON et al. (2003). Figure 18 shows the "RIM brightness," from which one can retrieve local clear-air reflectivity, observed at a single range gate on the morning of April 10, 2001.

While the so-called spatial-interferometry technique (PFISTER, 1971; WOODMAN, 1971) is the angular counterpart of FDI, the so-called coherent radar imaging (CRI) technique is the angular counterpart of RIM. CRI was first used in the upper atmosphere for the observation of plasma irregularities (KUDEKI and SÜRÜCÜ, 1991). PALMER et al. (1998) were the first to use CRI in the lower atmosphere.

4.3 Alternative perspectives by oversampling strategies

In Section 4.1, we have addressed the problem of how to find the optimum complex weights $w_j(\mathbf{x})$ for a given location $\mathbf{x}$ to be imaged. In this subsection, we outline a method to reconstruct the cross-covariance function $\langle n^*(\mathbf{x}')n(\mathbf{x}'')\rangle$ and not only its Bragg component.

In order to illustrate the basic idea, let us consider instead of (4.1) the following family of sampling functions

$$G_{lmn}(\mathbf{x}) = \frac{1}{\sqrt{\sigma_l}}A\left(\frac{\mathbf{r}_n+\mathbf{x}}{\sigma_l}\right)\exp\left[-i\beta_m(\mathbf{r}_0+\mathbf{r}_n+\mathbf{x})\right], \qquad (4.16)$$

where A stands for an admissible window or so-called analyzing function (e.g. Gaussian), $\mathbf{r}_n$ denotes the location, β_m the Bragg wavenumber, and σ_l (a dilation parameter) the pulse length. If one intends to reconstruct

$\langle n^*(\mathbf{x}')n(\mathbf{x}'')\rangle$, one has to make use of the sample values

$$\langle I^*_{lmn} I_{l'm'n'}\rangle = \int\int G^*_{lmn}(\mathbf{x}')G_{l'm'n'}(\mathbf{x}'')\times \times\langle n^*(\mathbf{x}')n(\mathbf{x}'')\rangle d\mathbf{x}'d\mathbf{x}''. \qquad (4.17)$$

The following observation illuminates the type of equation (4.17). For fixed σ_l (e.g. $\sigma_l = 1$ for all l) the integral transform is nothing more than the two-dimensional windowed Fourier transform evaluated at discrete points in the space–frequency domain, whereas for fixed β_m (4.17) results in the two-dimensional wavelet transform; for details we refer the reader to the very rich literature, e.g. DAUBECHIES (1992). For both situations there exists a well-developed theory on how to invert the integral equation. In the continuous framework (assume for a moment that the parameters σ, β, r, σ', β', and r' are continuously given) the inversion formula is in principle given by the adjoint integral operator; i.e.,

$$\langle n^*(\mathbf{x}')n(\mathbf{x}'')\rangle = \int \langle I^*_{\sigma\beta r} I_{\sigma'\beta' r'}\rangle \times \times G^*_{\sigma\beta r}(\mathbf{x}')G_{\sigma'\beta' r'}(\mathbf{x}'')d\mu(\sigma,\beta,r,\sigma',\beta',r'). \qquad (4.18)$$

Since our approach requires to deal with discrete parameter families $(\sigma_l, \beta_m, \mathbf{r}_n, \sigma_{l'}, \beta_{m'}, \mathbf{r}_{n'})$, we have to discretize this inversion formula in some adequate way. This leads directly to the so-called concept of frames (e.g., DUFFIN and SCHÄFER, 1952), i.e. to the discrete framework in which we are allowed to consider discrete families of parameters. The concept is well-understood for the Fourier as well as for the wavelet case; e.g., in the Fourier case the following family of functions

$$G_{l_0 mn}(\mathbf{x}) = \frac{1}{\sqrt{2\pi}\sigma_{l_0}} \exp\left(-\frac{(n\tilde{\mathbf{r}}+\mathbf{x})^2}{2\sigma^2_{l_0}}\right) \times \exp\left[-im\tilde{\beta}(\mathbf{r}_0 + n\tilde{\mathbf{r}} + \mathbf{x})\right]_{(m,n)\in\mathcal{I},\ \tilde{\beta}\tilde{\mathbf{r}}<2\pi} \qquad (4.19)$$

forms a frame, where $\mathcal{I}$ denotes an adequate index set. A Fourier-reconstruction formula is then given by

$$\langle n^*(\mathbf{x}')n(\mathbf{x}'')\rangle = \sum_{\substack{(m,n)\in\mathcal{I}\\(m',n')\in\mathcal{I}}} \langle I^*_{l_0 mn} I_{l_0' m'n'}\rangle \times \times \mathcal{D}(G^*_{l_0 mn}G_{l_0' m'n'})(\mathbf{x}',\mathbf{x}'') \ , \qquad (4.20)$$

where the system $\{\mathcal{D}(G^*_{l_0 mn}G_{l_0' m'n'})\}$ denotes the so-called dual frame which can be computed in some special situations exactly. In general, there exist several (linear as well as adaptive) schemes that approximate the dual frame very well. A similar formula can be established for the wavelet transform. However, for certain technical/physical reasons, the pure Gabor or the pure wavelet case might be too restrictive for our approach. In order to allow more flexibility in constructing an adequate analyzing frame, we have to relax the restrictions made on σ_l or β_m. To this end, we consider the non-restricted family

$$\left\{G^*_{\sigma_l\beta_m\mathbf{r}_n}G_{\sigma_{l'}\beta_{m'}\mathbf{r}_{n'}}\right\}_{(l,m,n,l',m',n')\in\mathcal{J}}. \qquad (4.21)$$

It is shown in DAHLKE et al. (2004a,b) that this family may form under certain assumptions on the sampling grid $\mathcal{J}$ a so-called mixed Gabor–wavelet–frame. It was pointed out that one can identify reasonable parameter families such that an increase of the sampling density with respect to $\{\sigma_l, \sigma_{l'}\}$ leads to a decrease of the redundancy with respect to $\{\beta_m, \beta_{m'}\}$ and vice versa (what is of course of practical impact). We obtain the following reconstruction scheme

$$\langle n^*(\mathbf{x}')n(\mathbf{x}'')\rangle = \sum_{(n,m,l,n',m',l')\in\mathcal{J}} \langle I^*_{nml} I_{n'm'l'}\rangle \times \times \mathcal{D}(G^*_{\sigma_n\beta_m\mathbf{r}_l}G_{\sigma_{n'}\beta_{m'}\mathbf{r}_{l'}})(\mathbf{x}',\mathbf{x}'') \ , \qquad (4.22)$$

where $\{\mathcal{D}(G^*_{\sigma_n\beta_m\mathbf{r}_l}G_{\sigma_{n'}\beta_{m'}\mathbf{r}_{l'}})\}_{(n,m,l,n',m',l')\in\mathcal{J}}$ stands again for the dual system. DAHLKE et al. (2004a,b) show how to construct or to approximate the dual frame function, or the so-called discrete reconstruction operator.

The whole concept of frame-based reconstruction schemes carries over to higher dimensions without essential changes. Moreover, the frame approach allows one to treat the reconstruction in a complete discrete setting, which is essential for fast numerical implementation. Note that the application of frame theory is strongly connected with incorporating oversampling (not only range oversampling). The main deficiency in the proposed method is that there might be a discrepancy between exact analytical inversion and the technical capabilities of radar devices. However, this results in the problem of identifying near-optimal parameter families, which requires of course a critical error analysis.

5 Summary and outlook

We have given a tutorial overview of concepts, problems, and solutions in advanced radar wind profiling (RWP). We have divided RWP into three categories: single-signal RWP, two-signal RWP, and multi-signal RWP.

Single-signal RWP, or traditional RWP, was pioneered thirty years ago (WOODMAN and GUILLÉN, 1974). Now it is a key technology for measuring winds and turbulence in the atmospheric boundary layer, the free troposphere, and the lower stratosphere. The vast majority of radar wind profilers (RWPs) used for research and operational purposes are single-signal RWPs.

The standard technique to retrieve vertical profiles of the three-dimensional wind vector from single-signal RWPs is the Doppler beam-swinging (DBS) technique. The standard tool for the statistical analysis of signal time series is the periodogram, from which the first three moments of the clear-air spectrum are estimated. We have discussed the problems of separating the clear-air signal, clutter, and noise. Based on a measured signal that was severely contaminated by clutter from an aircraft, we have discussed the potential of time-frequency decomposition techniques to efficiently remove airborne clutter.

Two-signal and multi-signal RWP offer a wealth of additional options to overcome limitations inherent in traditional RWP. An overview of recent progress in the physical and mathematical concepts and techniques of two-signal and multi-signal RWP has been given.

Given the need to observe meteorological fields reliably with higher spatial and temporal resolution, to design and optimize observational networks and make them adaptive to ever-changing observational needs, radar wind profiling will remain a fertile area of interdisciplinary research and development in the decades to come.

Acknowledgements

The authors thank Phil CHILSON, Jim JORDAN, Rich LATAITIS, and Bob PALMER for their helpful comments on earlier versions of this paper. Work on this paper begun when A. M. was with the University of Colorado at Boulder, Colorado and was affiliated with the NOAA Environmental Technology Laboratory. A. M.'s contribution was partially supported by the U. S. Army Research Office.

References

BALSLEY, B. B., M. L. JENSEN, R. G. FREHLICH, Y. MEILLIER, A. MUSCHINSKI, 2003: Extreme gradients in the nocturnal boundary layer: structure, evolution, and potential causes. – J. Atmos. Sci. **60**, 2496–2508.

BARTH, M. F., R. B. CHADWICK, D. VAN DE KAMP, 1994: Data processing algorithms used by NOAA's wind profiler demonstration network. – Ann. Geophysicae **12**, 518–528.

BATCHELOR, G. K., 1953: – The theory of homogeneous turbulence. – Cambridge University Press, Cambridge.

BOASHASH, B., 1992: Estimating and interpreting the instantaneous frequency of a signal - Part 1: Fundamentals. – Proc. IEEE **80**(4), 520–569.

BOISSE, J.-C., V. KLAUS, J.-P. AUBAGNAC, 1999: A wavelet transform technique for removing airplane echos from ST radar signals. – J. Atmos. Oceanic Technol. **16**, 334–346.

CHILSON, P. B., A. MUSCHINSKI, G. SCHMIDT, 1997: First observations of Kelvin-Helmholtz billows in an upper-level jet stream using VHF frequency domain interferometry. – Radio Sci. **32**, 1149–1160.

CHILSON, P. B., R. D. PALMER, A. MUSCHINSKI, D. A. HOOPER, G. SCHMIDT, H. STEINHAGEN, 2001: SOMARE-99: A demonstrational field campaign for ultra-high resolution VHF atmospheric profiling using frequency diversity. – Radio Sci. **36**, 695–707.

CHILSON, P. B., T.-Y. YU, R. G. STRAUCH, A. MUSCHINSKI, R. D. PALMER, 2003: Implementation and validation of range imaging on a UHF radar wind profiler. – J. Atmos. Oceanic Technol. **20**, 987–996.

COHEN, L., 1989: Time-frequency distributions – a review. – Proc. IEEE **77**(7), 941–981.

DAHLKE, S., G. STEIDL, G. TESCHKE, 2004a: Coorbit spaces and banach frames on homogeneous spaces with applications to analyzing functions on spheres. – Adv. Comput. Math. **21(1-2)**, 147–180.

DAHLKE, S., G. STEIDL, G. TESCHKE, 2004b: Weighted coorbit spaces and banach frames on homogeneous spaces. – J. Fourier Anal. Appl. **10**(5), 507–539.

DAUBECHIES, I., 1992: Ten Lectures on Wavelets. – SIAM, Philadelphia.

DOVIAK, R. J., R. J. LATAITIS, C. L. HOLLOWAY, 1996: Cross correlations and cross spectra for spaced antenna wind profilers — 1. Theoretical analysis. – Radio Sci. **31**, 157–180.

DOVIAK, R. J., D. S. ZRNIĆ, 1984: Reflection and scatter formula for anisotropically turbulent air. – Radio Sci. **19**, 325–336.

DOVIAK, R. J., D. S. ZRNIĆ, 1993: Doppler radar and weather observations, 2nd ed. – Academic Press, San Diego.

DUFFIN, R. J., A. C. SCHÄFER, 1952: A class of nonharmonic Fourier series. – Trans. Am. Math. Soc. **72**, 341–366.

FLANDRIN, P., 1999: Time-Frequency / Time-Scale Analysis. Wavelet Analysis and Its Applications. – Academic Press.

GABOR, D., 1946: Theory of communication. – J. Inst. Elec. Eng. **93** (III), 429–457.

GAGE, K. S., 1990: Radar observations of the free atmosphere: structure and dynamics. in D. Atlas, editor, – Radar in meteorology, Amer. Meteor. Soc., Boston, 534–565.

HILDEBRAND, P. H., R. S. SEKHON, 1974: Objective determination of the noise level in Doppler spectra. – J. Appl. Meteor. **13**, 808–811.

HLAWATSCH, F., G. BOUDREAUX-BARTELS, 1992: Linear and quadratic time-frequency signal representations. – IEEE Sig. Proc. Magazine, 21–67.

HOCKING, W. K., R. RÜSTER, P. CZECHOWSKY, 1986: Absolute reflectivities and aspect sensitivities of VHF radio wave scatterers measured with the SOUSY radar. – J. Atmos. Terr. Phys. **48**, 131–144.

Jordan, J. R., R. J. Lataitis, D. A. Carter, 1997: Removing ground and intermittent clutter contamination from wind profiler signals using wavelet transforms. – J. Atmos. Oceanic Technol. **14**, 1280–1297.

Jungnickel, D. (Ed.), 1999: Optimierungsmethoden. – Springer, Berlin, Heidelberg, Germany.

Justen, L., G. Teschke, V. Lehmann, 2004: Wavelet-based methods for clutter removal from radar wind profiler data. in F. Truchetet, editor, – Wavelet Applications in Industrial Processing Vol. 5266. The International Society for Optical Engineering, 157–168

Kolmogorov, A. N., 1941: Local structure of turbulence in an incompressible fluid at very high Reynolds numbers. – Dokl. Akad. Nauk SSSR **30**, 299–303.

Kudeki, E., G. Stitt, 1987: Frequency domain interferometry: a high resolution technique for studies of atmospheric turbulence. – Geophys. Res. Lett. **14**, 198–201.

Kudeki, E., F. Sürücü, 1991: Radar interferometric imaging of field-aligned plasma irregularities in the equatorial electrojet. – Geophys. Res. Lett. **18**, 41–44.

Lataitis, R. J., S. F. Clifford, C. L. Holloway, 1995: An alternative method for inferring winds from spaced-antenna radar measurements. – Radio Sci. **30**, 463–474.

Lehmann, V., G. Teschke, 2001: Wavelet based methods for improved wind profiler signal processing. – Ann. Geophysicae **19**, 825–836.

Luce, H., M. Crochet, F. Dalaudier, 2001a: Temperature sheets and aspect sensitive radar echoes. – Ann. Geophysicae **19**, 899–920.

Luce, H., M. Yamamoto, S. Fukao, D. Helal, M. Crochet, 2001b: A frequency domain radar interferometric imaging (FII) technique based on high resolution methods. – J. Atmos. Solar-Terr. Phys. **63**, 201–214.

Mallat, S., 1999: A Wavelet Tour Of Signal Processing. – Academic Press.

Muschinski, A., 1996: Possible effect of Kelvin-Helmholtz instability on VHF radar observations of the mean vertical wind. – J. Appl. Meteor. **35**, 2210–2217.

—, 1998: The first moments of the variance- and cross-spectra of standard and interferometric clear-air Doppler-radar signals. – NCAR Technical Note 441+STR, National Center for Atmospheric Research, Boulder, Colorado.

—, 2004: Local and global statistics of clear-air Doppler radar signals. – Radio Sci. **39**, RS1008, Doi:10.1029/2003RS002908.

Muschinski, A., D. H. Lenschow, 2001: Future directions for research on meter- and submeter-scale, atmospheric turbulence. – Bull. Amer. Meteor. Soc. **82**, 2831–2843.

Muschinski, A., C. Wode, 1998: First in situ evidence for coexisting submeter temperature and humidity sheets in the lower free troposphere. – J. Atmos. Sci. **55**, 2893–2906.

Muschinski, A., P. B. Chilson, S. Kern, J. Nielinger, G. Schmidt, T. Prenosil, 1999: First frequency-domain interferometry observations of large-scale vertical motion in the atmosphere. – J. Atmos. Sci. **56**, 1248–1258.

Muschinski, A., P. B. Chilson, R. D. Palmer, G. Schmidt, H. Steinhagen, 2001: Boundary-layer convection and diurnal variation of vertical-velocity characteristics in the free troposphere. – Quart. J. Roy. Meteor. Soc. **127**, 423–443.

Nastrom, G. D., T. E. VanZandt, 1994: Mean vertical motion seen by radar wind profilers. – J. Appl. Meteor. **33**, 984–995.

Ottersten, H. A., 1969: Radar backscattering from the turbulent clear atmosphere. – Radio Sci. **4**, 1251–1255.

Palmer, R. D., P. B. Chilson, A. Muschinski, G. Schmidt, T.-Y. Yu, and H. Steinhagen, 2001: SOMARE-99: Observations of tropospheric scattering layers using multiple-frequency range imaging. – Radio Sci. **36**, 681–693.

Palmer, R. D., S. Gopalam, T.-Y. Yu, S. Fukao, 1998: Coherent radar imaging using Capon's method. – Radio Sci. **33**, 1585–1598.

Palmer, R. D., T.-Y. Yu, P. B. Chilson, 1999: Range imaging using frequency diversity. – Radio Sci. **34**, 1485–1496.

Pfister, W., 1971: The wave-like nature of inhomogeneities in the e-region. – J. Atmos. Terr. Phys. **33**, 999–1025.

Röttger, J., M. F. Larsen, 1990: UHF/VHF radar techniques for atmospheric research and wind profiler applications. in D. Atlas, editor, – Radar in meteorology pp. 235–281. Amer. Meteor. Soc., Boston.

Strauch, R. G., D. A. Merritt, K. P. Moran, K. B. Earnshaw, D. van de Kamp, 1984: The Colorado wind profiling network. – J. Atmos. Oceanic Technol. **1**, 37–49.

Tatarskii, V. I., 1961: – Wave propagation in a turbulent medium. – McGraw-Hill, New York.

—, 2003: Theory of single scattering by random distributed scatterers. – IEEE Trans. Ant. Prop. **51**, 2806–2813.

Tatarskii, V. I., A. Muschinski, 2001: The difference between Doppler velocity and real wind velocity in single scattering from refractive index fluctuations. – Radio Sci. **36**, 1405–1423.

Weber, B. L., D. B. Wuertz, D. C. Law, A. S. Frisch, J. M. Brown, 1992: Effects of small-scale vertical motion on radar measurements of wind and temperature profiles. – J. Atmos. Oceanic Technol. **9**, 193–209.

WOODMAN, R. F., 1971: Inclination of the geomagnetic field measured by an incoherent scatter technique. – J. Geophys. Res. **76**, 178–184.

WOODMAN, R. F., A. GUILLÉN, 1974: Radar observations of winds and turbulence in the stratosphere and mesosphere. – J. Atmos. Sci. **31**, 493–505.

YAMAMOTO, M. K., F. FUJIWARA, T. HORINOUCHI, H. HASHIGUCHI, S. FUKAO, 2003: Kelvin-Helmholtz instability around the tropical tropopause observed with the Equatorial Atmosphere Radar. – Geophys. Res. Lett. **30**, 1476, Doi:10.1029/2002GL016685. Erratum: Geophys. Res. Lett. **30**, 1716, Doi:10.1029/2003GL017791.